

CHEMISTRY

Self-assembly-induced luminescence of Eu^{3+} -complexes and application in bioimaging

Ping-Ru Su¹, Tao Wang¹, Pan-Pan Zhou¹, Xiao-Xi Yang¹, Xiao-Xia Feng¹, Mei-Na Zhang¹, Li-Juan Liang¹, Yu Tang^{1,2,*} and Chun-Hua Yan^{1,*}

ABSTRACT

Design and engineering of highly efficient emitting materials with assembly-induced luminescence, such as room-temperature phosphorescence (RTP) and aggregation-induced emission (AIE), have stimulated extensive efforts. Here, we propose a new strategy to obtain size-controlled Eu^{3+} -complex nanoparticles (Eu-NPs) with self-assembly-induced luminescence (SAIL) characteristics without encapsulation or hybridization. Compared with previous RTP or AIE materials, the SAIL phenomena of increased luminescence intensity and lifetime in aqueous solution for the proposed Eu-NPs are due to the combined effect of self-assembly in confining the molecular motion and shielding the water quenching. As proof of concept, we also show that this system can be further applied in bioimaging, temperature measurement and HClO sensing. The SAIL activity of the rare-earth (RE) system proposed here offers a further step forward on the roadmap for the development of RE light conversion systems and their integration in bioimaging and therapy applications.

Keywords: rare earth complexes, self-assembly-induced luminescence, bioimaging, temperature and HClO sensing

INTRODUCTION

The unique properties of rare-earth (RE) complexes including ligand-sensitized energy transfer, fingerprint-like emissions and long-lived emissions [1–3], make them promising materials for many applications such as LED devices [4,5], optical encoding [6,7], luminescence imaging/detection [8–11] and time-resolved luminescence detection [12,13]. In particular, the use of RE luminescent materials for *in vitro* and *in vivo* imaging can easily eliminate the autofluorescence of organisms and any interference from background fluorescence [14]. However, most RE complexes have poor solubility and stability in aqueous solution and their luminescence can be easily quenched by nearby X–H (X = O, N, C) oscillators [15–17], which limits their further application in aqueous solutions and bioimaging. Consequently, improving their luminescence performance as well as dispersibility has become a key issue in expanding the application of RE complexes. Until now, extensive efforts have been devoted to increasing the luminescence intensity of RE complexes,

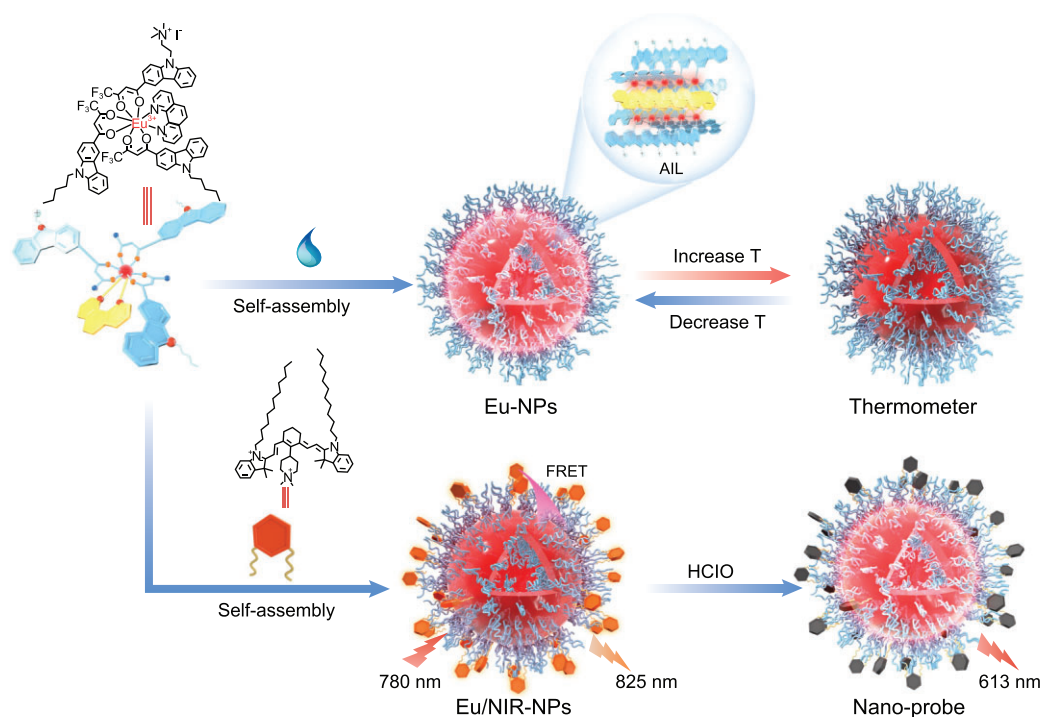
such as increasing structural rigidity, adjusting coordination numbers, replacing ligand C–H bonds with C–F bonds and changing the electron-donating or electron-withdrawing characteristics of substituents [18–20].

Recently, assembly-induced emission materials, such as room-temperature phosphorescence (RTP) materials and aggregation-induced emission (AIE) luminogens (AIEgens), have become research hotspots [21–24]. Ma *et al.* summarized the recent advances in assembly-induced emission of amorphous RTP materials [25]. Tang *et al.* summarized the progress of AIE and its related fields, and suggested its application prospects in materials and biological sciences [26]. Compared to these emitting materials, RE complexes have a relatively complicated sensitized luminescence mechanism. In different sensitization processes, the energy transfer from the excited triplet state of the ligands to the excited state of the RE ions ($T_1\text{-RE}^*$) is the main cause of sensitization [27]. Therefore, increasing the possibility of intersystem crossing to the ligand triplet

¹State Key Laboratory of Applied Organic Chemistry, Key Laboratory of Nonferrous Metal Chemistry and Resources Utilization of Gansu Province, College of Chemistry and Chemical Engineering, Lanzhou University, Lanzhou 730000, China and ²State Key Laboratory of Baiyunobo Rare Earth Resource Researches and Comprehensive Utilization, Baotou Research Institute of Rare Earths, Baotou 014030, China

*Corresponding authors. E-mails: tangyu@lzu.edu.cn; yan@lzu.edu.cn

Received 29 September 2020;
Revised 18 January 2021; Accepted 18 January 2021



Scheme 1. Schematic illustration of the synthetic protocol of the self-assembly-induced luminescence (SAIL) of Eu-complex and its application for the bioimaging of temperature and HClO.

excited state (S_1-T_1) and reducing the non-radiative decay would be beneficial to the luminescence of RE complexes.

Recent studies have shown that supramolecular assembly can build highly water-dispersible nanostructures through non-covalent intermolecular force, which would allow the RE complex to be applied in more areas [28–30]. Kimizuka *et al.* encapsulated Eu³⁺-complexes into amphiphilic matrices to reduce the quenching of water molecules and increase the stability of complexes by supramolecular assembly [31]. With an organic–inorganic assembling strategy, Li *et al.* also used RE complexes as emitting sources to realize robust luminescent hydrogels [32]. However, it is difficult to predict the assembly and to control the particle size distribution by simply dispersing RE complexes into host matrices. As known, self-assembly driven by intermolecular forces, such as hydrophobic–hydrophobic, hydrogen bonding and aromatic π – π stacking, has a high degree of orientation and predictability, and is a powerful strategy for synthesizing nanostructures with precise sizes and shapes [33]. At the same time, such intermolecular interaction forces can change the intermolecular distance, limit the rotation of the ligand molecules and regulate the energy transfer from the ligands to the central RE ions [34].

Here, a new strategy was proposed to obtain size-controlled Eu³⁺-complex nanoparticles (Eu-NPs) with self-assembly-induced luminescence

(SAIL) characteristics without encapsulation or hybridization. The amphiphilic Eu³⁺-complex (Eu(THB)(THA)₂Phen) possessing carbazole derivative ligands, with highly π – π conjugated electron structure, could self-assemble into Eu-NPs with excellent water dispersibility and controllable particle size in aqueous solution (Scheme 1). We envisaged that adjusting the molecular polarity of the ligands and transferring the RE complexes from the organic phase to the water phase could cause the RE complexes to assemble into NPs with good water dispersibility. By studying the changes in luminescence lifetimes and quantum yields in aqueous solution, we found that (i) self-assembly could effectively shield the water molecules in the luminescent center and thus reduce the quenching effect of the water molecules from the vibration of the O–H bond; (ii) when the molecules are self-assembled together, they restrain each other, and their movement within the molecules is restricted. This will greatly limit the intramolecular rotation or vibration of Eu³⁺-complexes, thus resulting in the enhancement of luminescence in aqueous conditions. Also, this system could be used for bioimaging application for the detection of temperature and HClO by steady-state fluorescence and time-resolved assay as shown in Scheme 1. We believe that the SAIL activity of the self-assembled RE complexes system proposed here paves a new way for the development of RE light conversion

systems and their integration in bioimaging and therapy applications.

RESULTS AND DISCUSSION

Self-assembly morphology and properties of Eu^{3+} -complexes in aqueous solution

First, we successfully synthesized hydrophilic ligand N,N,N -trimethyl-2-(3-(4,4,4-trifluoro-3-oxobutanyloxy)-9H-carbazol-9-yl)ethan-1-aminium (HTHB) (Scheme S1) and hydrophobic ligand 4,4,4-trifluoro-1-(9-pentyl-9H-carbazol-3-yl) butane-1,3-dione (HTHA) (Scheme S2). The synthetic steps and ^1H and ^{13}C NMR spectra are listed in the supporting information. Then, a new amphiphilic Eu^{3+} -complex ($\text{Eu}(\text{THB})(\text{THA})_2\text{Phen}$, Scheme S3) was synthesized according to our previous work [35]. The successful synthesis of Eu^{3+} -complex was confirmed by high resolution mass spectrometry (HRMS), MALDI-TOF and elemental analysis as shown in the supporting information.

The self-assembly behavior of $\text{Eu}(\text{THB})(\text{THA})_2\text{Phen}$ in aqueous solution was studied by dissolving the Eu^{3+} -complexes in a small amount of acetone, and then dispersing them into aqueous solution with ultrasound treatment. Transmission electron microscopy (TEM) images showed that the $\text{Eu}(\text{THB})(\text{THA})_2\text{Phen}$ complex self-assembled into novel spherical micelle NPs (Eu-NPs) with a double-layer structure (Fig. 1a and b). To expand the application of Eu-NPs in constructing Förster resonance energy transfer (FRET) systems, we also co-assembled $\text{Eu}(\text{THB})(\text{THA})_2\text{Phen}$ with amphiphilic near-infrared dye IR-780. The TEM images showed that they could also be co-assembled into nanospheres with uniform morphology and good dispersion (Fig. 1c). The elemental mapping of Eu^{3+} -NPs showed that F, O, Eu, N and C elements were evenly distributed on the vesicles (Fig. 1d). The energy dispersive spectroscopy (EDS) spectrum of Eu-NPs further confirmed the existence of these elements (Fig. S1).

To study the influence of $\text{Eu}(\text{THB})(\text{THA})_2\text{Phen}$ concentration on the self-assembly of nanoparticles, scanning electron microscopy (SEM) images were collected and particle size distribution of Eu-NPs was measured at different concentrations of $\text{Eu}(\text{THB})(\text{THA})_2\text{Phen}$ (0.005 mM, 0.01 mM, 0.02 mM, 0.04 mM, 0.06 mM, 0.8 mM, 0.1 mM, 0.2 mM, 0.3 mM, 0.4 mM, 0.5 mM, 0.6 mM, 0.7 mM, 0.8 mM, 0.9 mM and 1.0 mM). It was found from SEM images (Fig. 1e and f

and Fig. S2) that $\text{Eu}(\text{THB})(\text{THA})_2\text{Phen}$ assembled more efficiently in aqueous solution with increasing concentration, and the particle size and dispersion of Eu-NPs gradually increased. The confocal microscope images (Fig. 1g) showed that Eu-NPs had good dispersibility and luminescence properties. The results of dynamic light scattering (DLS) analysis (Fig. 1h) showed that the average hydrodynamic diameter of Eu-NPs at different concentrations of $\text{Eu}(\text{THB})(\text{THA})_2\text{Phen}$ (from 0.10 mM to 1.0 mM) increased from 56 ± 5 nm to 245 ± 5 nm. $\text{Eu}(\text{THB})(\text{THA})_2\text{Phen}$ self-assembled more efficiently in aqueous solution with increasing concentration and its luminescence intensity increased with the increase in its concentration (Fig. 1i). We labeled Eu^{3+} -NPs at different concentrations of $\text{Eu}(\text{THB})(\text{THA})_2\text{Phen}$ (from 0.10 mM to 1.0 mM) as Eu-NPs-0.1 to Eu-NPs-1.0. By comparing the changes in X-ray photoelectron spectroscopy (XPS) data before and after the self-assembly of $\text{Eu}(\text{THB})(\text{THA})_2\text{Phen}$, it was further verified that the same elements were present before and after self-assembly (Fig. 1j). To assess the universality of the proposed self-assembly strategy, we also synthesized three other Eu^{3+} -complexes, including $\text{Eu}(\text{THA})_3\text{Phen}$, $\text{Eu}(\text{tta})_3(\text{dpqt})$ and $\text{Eu}(\text{THA})_3(\text{dpqt})$ (Schemes S5–S8) and studied their self-assembly property. As shown in Fig. S3, they all assembled into NPs with different morphologies in aqueous solution. Furthermore, RE complexes are often coordinated competitively by other molecules, such as PO_4^{3-} , amino acids, etc., which can affect the luminescence. To study whether self-assembly increases the resistance of RE complexes to interference by other molecules, interference experiments were conducted. The results showed that other substances (H_2PO_4^- , NO_2^- , HPO_4^{2-} , HCO_3^- , CO_3^{2-} , SO_4^{2-} , PO_4^{3-} , HSO_3^- , SCN^- , CN^- , PBS, GSH, Asp, Arg, Cys) did not interfere noticeably with the fluorescence of the self-assembled nanoparticles Eu-NPs-1.0 (Fig. S4). We also studied the shelf stability of Eu-NPs-1.0 in aqueous solution, and found that it is very stable in aqueous solution (Fig. S5).

In order to further investigate the self-assembly behavior, calculations were carried out using the periodic density functional theory (DFT) method and the local-density approximation (LDA). In the optimized structure of $\text{Eu}(\text{THB})(\text{THA})_2\text{Phen}$, the carbazole ring of the HTHA group was in a plane, while the carbazole ring of HTHB was on the opposite side of HTHA (Fig. S6a). From the optimized structure of molecular stacking, it can be seen that the molecules are stacked in antisymmetric manner. The distance between the mass centers of the carbazole rings of the ligand HTHB was 3.786 Å,

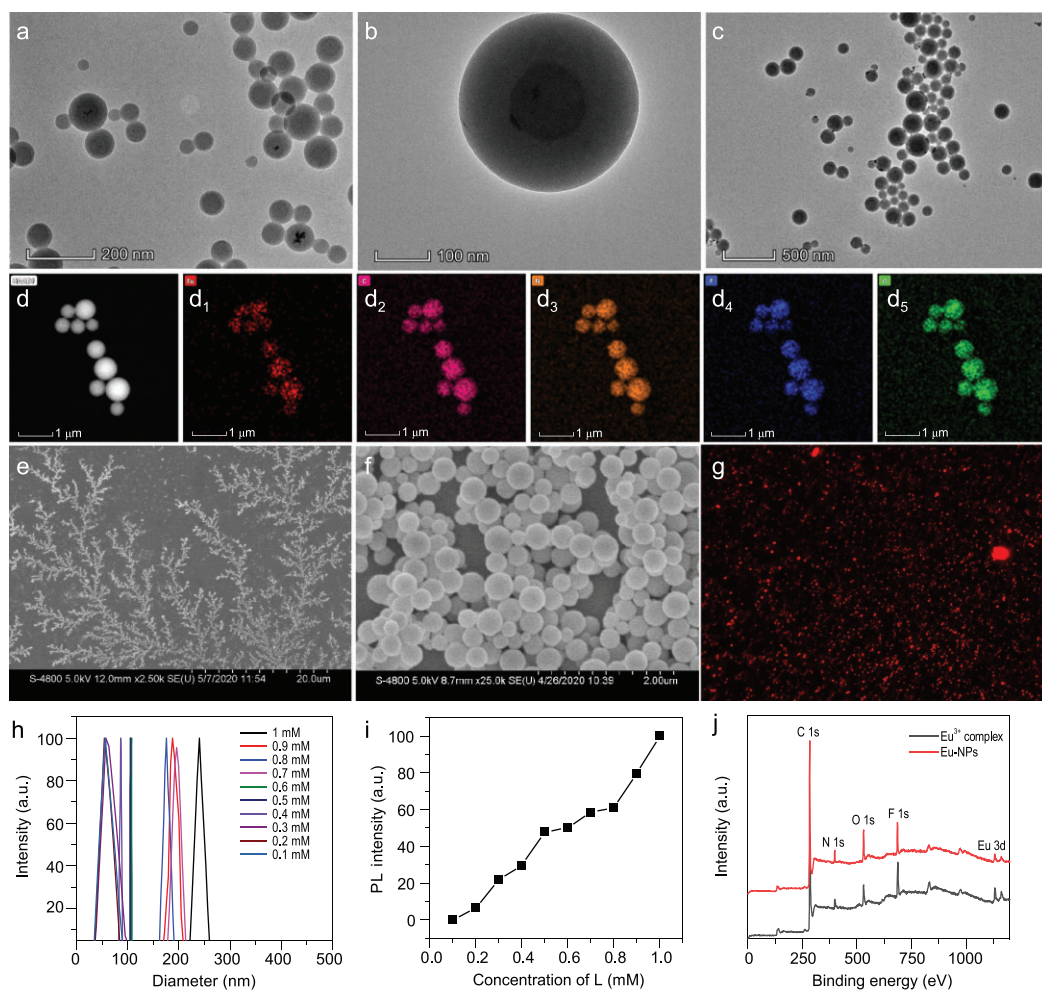


Figure 1. (a and b) TEM images of Eu-NPs at the concentrations of 0.5 mM. (c) TEM images of Eu/NIR-NPs. (d) The elemental mapping images of Eu-NPs. (e and f) SEM images of Eu-NPs at different concentrations of 0.005 and 1 mM. (g) Confocal fluorescence microscope images of Eu-NPs at the concentration of 1 mM ($\lambda_{\text{ex}} = 405$ nm; $\lambda_{\text{em}} = 600\text{--}640$ nm). (h) Hydrodynamic particle size distribution of Eu-NPs at different concentrations from 0.1 to 1 mM in aqueous solution measured by DLS. (i) Normalized luminescence intensity of Eu-NPs with different size distributions (the total Eu^{3+} -complexes remained the same). (j) XPS spectra of $\text{Eu}(\text{THB})(\text{THA})_2\text{Phen}$ and Eu-NPs.

which indicated that there was a π - π stacking force in the molecular aggregation (Fig. S6b). Therefore, the non-covalent forces that induce Eu^{3+} -complexes to self-assemble into Eu-NPs are hydrophobic-hydrophobic, hydrogen bonding and aromatic π - π stacking forces.

Photoluminescence and UV-vis spectra of Eu^{3+} -complexes in binary solvents of organic and water

The luminescence of the Eu^{3+} -complexes was studied in mixed solutions of organic solvents (THF, MeCN, ethanol, DMSO, DMF and acetone) and water. We investigated the luminescence changes of the four Eu^{3+} -complexes (25 μM)

($\text{Eu}(\text{THB})(\text{THA})_2\text{Phen}$, $\text{Eu}(\text{THA})_3\text{Phen}$, $\text{Eu}(\text{tta})_3(\text{dpqt})$ and $\text{Eu}(\text{THA})_3(\text{dpqt})$) (Fig. S7a₁-c₁) in varying proportions of acetone/water binary mixtures by adding acetone solution to water followed by stirring for 5 min. As shown in Fig. 2a and b and Fig. S7a₂-c₃, when $V_{\text{H}_2\text{O}} < 40\%$, the luminescent intensities of Eu^{3+} at emission wavelength of 613 nm (${}^5\text{D}_0 \rightarrow {}^7\text{F}_2$) decreased slightly, which could be attributed to the increased quenching of the luminescence of Eu^{3+} through the excitation of O-H vibrations. Interestingly, when $V_{\text{H}_2\text{O}} > 40\%$, the luminescent intensities sharply increased. On the contrary, with the increase in water content, the ligand fluorescence of complexes $\text{Eu}(\text{tta})_3(\text{dpqt})$ and $\text{Eu}(\text{THA})_3(\text{dpqt})$ at emission wavelength of 460 nm was quenched by the well-known aggregation-caused quenching (ACQ)

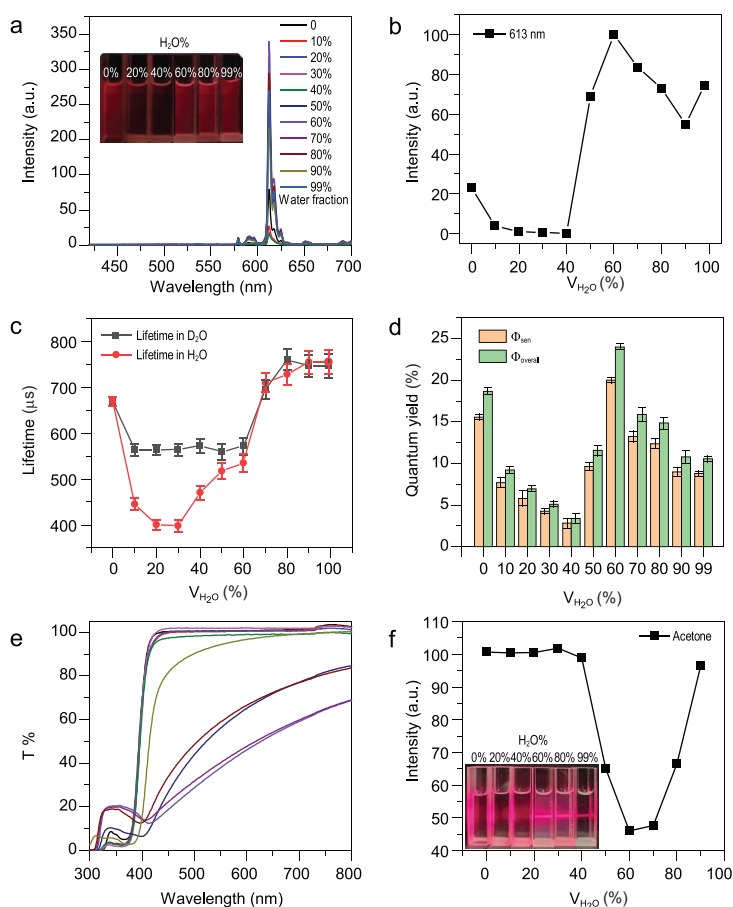


Figure 2. (a) Photoluminescence spectra of Eu(THB)(THA)₂Phen (50 μM) in acetone/water mixtures (inset: fluorescent photographs of Eu(THB)(THA)₂Phen at different water fractions). (b) The normalized luminescence intensity of Eu(THB)(THA)₂Phen (50 μM) in acetone/water mixtures. (c) The lifetime at the wavelength of 613 nm for Eu(THB)(THA)₂Phen (50 μM) in different acetone/D₂O (black line) or acetone/H₂O (red line) mixtures. (d) Luminescence quantum yield (Φ_{overall}) and the efficiency of energy transfer (Φ_{sen}) from ligand to Eu³⁺ ions of Eu(THB)(THA)₂Phen (50 μM) in different acetone/water mixtures. (e and f) Dependence of the optical transmittance at 600 nm of Eu(THB)(THA)₂Phen in different acetone/water mixtures (inset: photographs of Eu³⁺ complexes at different water fractions and their Tyndall effect).

effect [36]. Besides, when the excitation wavelength and concentration of Eu(THB)(THA)₂Phen (5.0 μM, 25.0 μM, 50.0 μM, 100.0 μM) were varied, the change in luminescence intensity showed the same phenomenon (Figs S8 and S9). Nevertheless, the luminescence slightly decreased when water fraction exceeded 60%. This was because the particle size became smaller with increasing water content (Fig. S10), which lowered the number of self-assembled Eu³⁺-complexes [29].

We assumed that the enhancement of luminescence was due to the self-assembly of Eu³⁺-complexes as the amount of water increased. Therefore, the luminescent center was likely hidden in the hydrophobic cavity, reducing the influence of the surrounding water on its luminescence.

To verify our hypothesis, the number of water molecules in the first coordination sphere of Eu³⁺ ions in Eu(THB)(THA)₂Phen was estimated by using the following equation (1) [37]

$$q = 1.2 (\tau_H^{-1} - \tau_D^{-1} - 0.25), \quad (1)$$

where q represents the number of coordinated water molecules, and τ_H and τ_D are the luminescence lifetimes measured in H₂O and D₂O, respectively. Using this formula, it was determined that the number of coordinated water molecules q in Eu(THB)(THA)₂Phen was 0.6 ± 0.1 , indicating that almost one water molecule was coordinated with two Eu³⁺ ions in Eu(THB)(THA)₂Phen. In contrast, when the proportion of water exceeded 60%, the luminescence decay rate of Eu(THB)(THA)₂Phen in H₂O was only slightly lower than that in D₂O, which proved that the number of coordinated water molecules in the first coordination sphere of Eu³⁺ ions in Eu(THB)(THA)₂Phen was very small (Fig. 2c). However, in the system of D₂O/acetone, when the water content was greater than 40%, the fluorescence lifetime still showed an increasing trend, which indicated that excluding the quenching effect of water molecules was not the only reason for the enhanced fluorescence. Therefore, it can be argued that the self-assembly leads to physical and spatial limitations, which greatly hinder the intramolecular rotation or vibration of the Eu³⁺-complex, resulting in enhanced luminescence under aqueous conditions.

The quantum yields (Φ) of Eu(THB)(THA)₂Phen were studied in varying proportions of acetone/water binary mixtures. The overall luminescence quantum yield (Φ_{overall}) followed the same trend as the luminescence intensity (Fig. 2d and Table S1), which increased from $(3.4 \pm 0.1)\%$ to $(24.0 \pm 0.1)\%$ when the water fraction increased from $(40.0 \pm 0.1)\%$ to $(60.0 \pm 0.1)\%$. We also studied the efficiency of the energy transfer (Φ_{sen}) from ligand to Eu³⁺ ions of Eu(THB)(THA)₂Phen (50 μM) in different acetone/water mixtures. The relationship between Φ_{overall} and Φ_{sen} can be expressed by the following formula (2) [38],

$$\Phi_{\text{overall}} = \Phi_{\text{sen}} \Phi_{\text{Eu}}. \quad (2)$$

The intrinsic quantum yield of Eu³⁺ (Φ_{Eu}) was estimated by the following equation (3), and it is assumed that the decay process at 77 K in deuterated solvents is purely radiative [39,40],

$$\Phi_{\text{Eu}} = \tau_{\text{obs}}(298 \text{ K}) / \tau_{\text{obs}}(77 \text{ K}). \quad (3)$$

The changes of Φ_{sen} in different acetone/water ratios demonstrated the inherent reason for the changes in fluorescence intensity. The calculation results showed that the change trend of Φ_{sen} was consistent with the fluorescence intensity. At the same time, the internal quantum yield increased from $(9.6 \pm 0.1)\%$ (water 40%) to $(20.0 \pm 0.1)\%$ (water 60%) (Table S1). This further proved that the assembly greatly limited the intramolecular rotation or vibration of Eu^{3+} complexes, which facilitated energy transfer from the ligand to the central Eu^{3+} ions.

We also studied the change in luminescence or light transmittance of $\text{Eu}(\text{THB})(\text{THA})_2\text{Phen}$ in other mixed solutions of organic solvents (THF, MeCN, ethanol, DMSO and DMF) and water. The general trend of luminescence change was the same as that in the acetone/water mixed solvent, but the sharp change in fluorescence or light transmittance occurred at different proportions of water component (Figs S11 and S12). This may be caused by the fact that the solubility of $\text{Eu}(\text{THB})(\text{THA})_2\text{Phen}$ differs in different organic solvents/water. By measuring the change in light transmittance at 600 nm in different acetone/water ratios, it was found that the light transmittance decreased significantly when water fraction was greater than 40% (Fig. 2e and f). Turbidity and Tyndall effect were also observed from photographs of Eu^{3+} complexes at water fraction >40% (inset of Fig. 2f). These experimental results provided further evidence for the self-assembly of the Eu^{3+} -complexes when the water ratio was greater than 40%. When the proportion of water was greater than 60%, its light transmittance began to increase again. This was consistent with a slight decrease in fluorescence intensity, further confirming that the assembled particles became smaller and the number of effective assemblies was reduced.

Temperature-sensing performance of Eu-NPs

With the rapid development of scientific research, technology applications and industrial production, traditional thermometers cannot meet the requirements for measurement of temperature in some particular areas, including micron- or nanodevices, biological processes and disease diagnoses [41]. In addition, accurate detection of the temperature distribution of living cells, especially the temperature distribution of cancer cells that have higher temperature than normal tissues due to the increased metabolic activity, could greatly enhance the understanding of their pathology and physiology, thereby optimizing diagnoses and treatment processes (for example, in hyperthermia tumor treatment and

photodynamic therapy) [42,43]. Therefore, it is urgent to develop nanoscale temperature measurement devices to achieve temperature measurement of specific lesions. At the same time, controlling the characteristics of nanomaterials (for example, size dispersion, surface modification) can help achieve different spatial resolutions and positioning.

So far, there is no report on the application of self-assembled RE complexes as nanometer thermometers. In order to study the response of the Eu-NPs to temperature changes, we selected Eu-NPs-0.5 as a nanothermometer and measured its steady-state luminescence and transient-state luminescence at different temperatures (Fig. 3a). As shown in Fig. 3b, the luminescence intensity of ${}^5\text{D}_0-{}^7\text{F}_2$ transition (I_{613}) reduced as the temperature increased. The linear relationship between temperature and I_{613} could be fitted as a function of equation (4)

$$I_{613} = 314.864 - 4.23 T, \quad (4)$$

with a correlation coefficient (R^2) of 0.997 (Fig. 3c). Quantitative comparison of thermometers operated by different mechanisms can be performed using relative sensitivity, which is defined as equation (5),

$$S = \left| \frac{\partial (I_{613}) / \partial (T)}{I_{613}} \right|. \quad (5)$$

The fluorescence lifetime value has good stability, and it does not depend on the penetration depth of biological tissue, the concentration of the probe, light scattering, reflection or the intensity fluctuation of the excitation source. Thus, it breaks through the limitations of traditional steady-state fluorescence detection, adding an independent new dimension of information to fluorescence imaging. Compared with traditional organic fluorescent probes, RE complexes as nanoprobables have unique photophysical advantages, including longer emission lifetimes and time-gated and time-resolved measurements. Therefore, we measured the change in luminescence lifetime of ${}^5\text{D}_0-{}^7\text{F}_2$ (613 nm) induced by the change in temperature from 25°C to 70°C to evaluate the potential application of Eu-NPs-0.5 as a lifetime thermal sensor. Figure 3d shows the luminescence decay curve of Eu-NPs-0.5 from 25°C to 70°C, which indicates that the luminescence lifetime of ${}^5\text{D}_0-{}^7\text{F}_2$ (613 nm) decreased with increasing temperature. The linear relationship between the luminescence decay time (τ_{613}) and temperature indicated that the luminescence lifetime and temperature (from 24°C to 45°C) had a good linear relationship with the correlation coefficient (R^2) of 0.986 (Fig. 3e). The linear relationship between temperature and luminescence decay time (τ_{613}) could

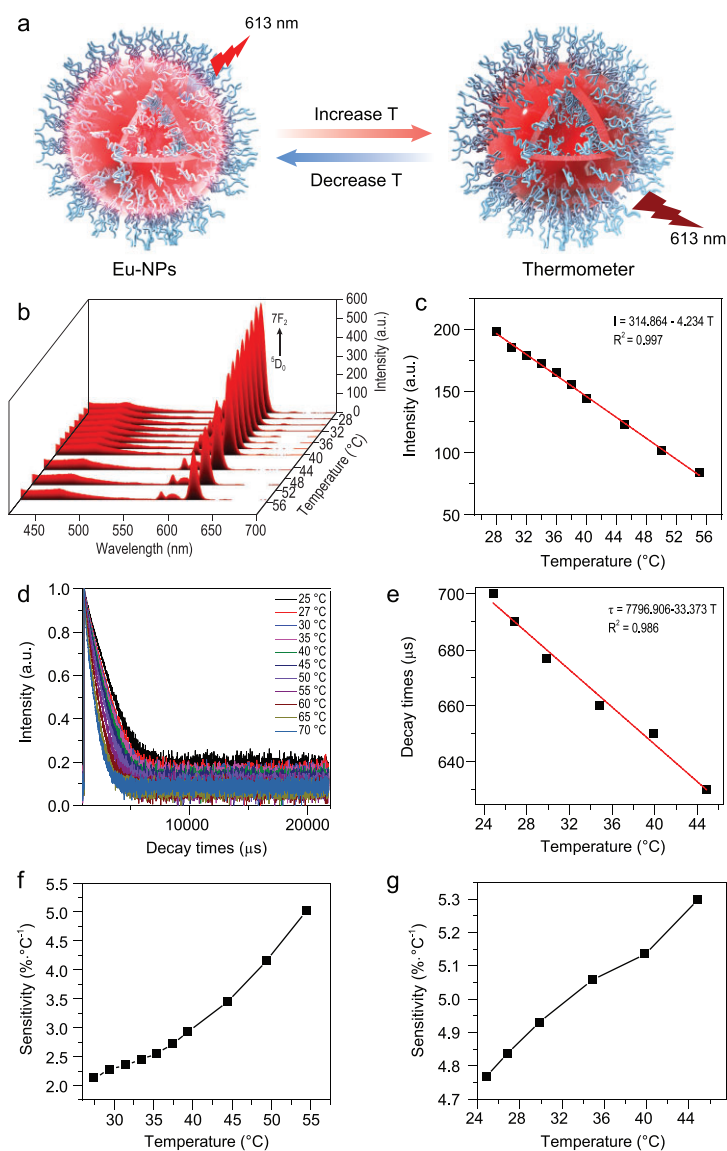


Figure 3. (a) Schematic illustration of Eu-NPs sensing temperature. (b) Photoluminescence spectra of Eu-NPs-0.5 at different temperatures in water media. (c) The linear relationship between the luminescence intensity ($\lambda_{em} = 613$ nm) and different temperatures in water (from 24°C to 55°C). (d) The decay curves at the wavelength of 613 nm for Eu-NPs-0.5 at different temperatures. (e) The linear relationship between the luminescence decay time (τ_{613}) and different temperature (from 24°C to 45°C). (f) The relative sensitivity (S_r) for Eu-NPs-0.5. (g) The relative sensitivity (S_r) of temperature-dependent lifetime for Eu-NPs-0.5.

be fitted as a function of the following equation (6),

$$\tau_{613} = 7796.906 - 33.373T. \quad (6)$$

Figure 3f revealed that the maximum relative sensitivity and the minimum relative sensitivity were $5.1\% \cdot ^\circ\text{C}^{-1}$ and $2.3\% \cdot ^\circ\text{C}^{-1}$ at 55.0°C and 25°C , respectively. It indicated that Eu-NPs-0.5 can be applied as a thermal sensor to situations that require precise temperature measurement.

As shown in Fig. 3g, the maximum relative sensitivity and the minimum relative sensitivity were $5.3\% \cdot ^\circ\text{C}^{-1}$ and $4.75\% \cdot ^\circ\text{C}^{-1}$ at 45.0°C and 25°C , respectively. It indicated that Eu-NPs-0.5 can be applied as a thermal sensor to situations that require precise temperature measurement. The maximum relative sensitivity of Eu-NPs was higher than that of other reported RE thermal probes (Table S2).

For fluorescent probes used as temperature sensors, thermal stability is also critical. The thermal stability of Eu-NPs-0.5 has been studied by TGA-DSC technology. Figure S13 shows that the melting point and decomposition temperature were 208°C and 337°C , respectively. Thus, Eu-NPs-0.5 has good thermal stability and can be used as a temperature sensor. At the same time, we also studied the temperature measurement properties of high and low temperature cycles, and found that Eu-NPs-0.5 has good cycling properties for temperature measurement (Fig. S14). We studied the particle size distribution of the Eu-NPs-0.5 at different temperatures (from 25°C to 55°C), and found that the particle size did not change significantly with the temperature change, which showed that the temperature change within the measured temperature range cannot destroy the assembly (Fig. S15).

Application in sensing of HClO

Hypochlorous acid (HClO) is produced by hydrogen peroxide and chloride ions under the catalytic action of myeloperoxidase (MPO) in the body. Growing attention is given to the identification and detection of HClO, due to its vital role in bioassay of physiological processes, such as cell differentiation, migration, conduction and immunity, etc. [44]. The FRET-based fluorescent probes have the advantages of a large Stokes shift, ratiometric sensing, dual/multi-analyte responsive systems, etc., which have gained strong research interest [45]. At the same time, most near-infrared fluorescent dyes are prone to fluorescent photobleaching, and most HClO fluorescent probes are Turn-Off type, which is not conducive to accurate and sensitive detection. Here, based on the FRET system constructed by HClO fluorescent probe IR-780 and Eu^{3+} complexes, ratiometric HClO luminescence nanoprobe Eu/NIR-NPs was constructed by co-assembly, in which two-photon-sensitized amphiphilic $\text{Eu}(\text{THB})(\text{THA})_2\text{Phen}$ directly co-assembled with cationic IR-780 (Fig. 4a). Based on the good overlap between the emission peaks of $\text{Eu}(\text{THB})(\text{THA})_2\text{Phen}$ and the strong absorption of IR-780, (Eu/NIR-NPs) and $\text{Eu}(\text{THB})(\text{THA})_2\text{Phen}$ were used as energy donors

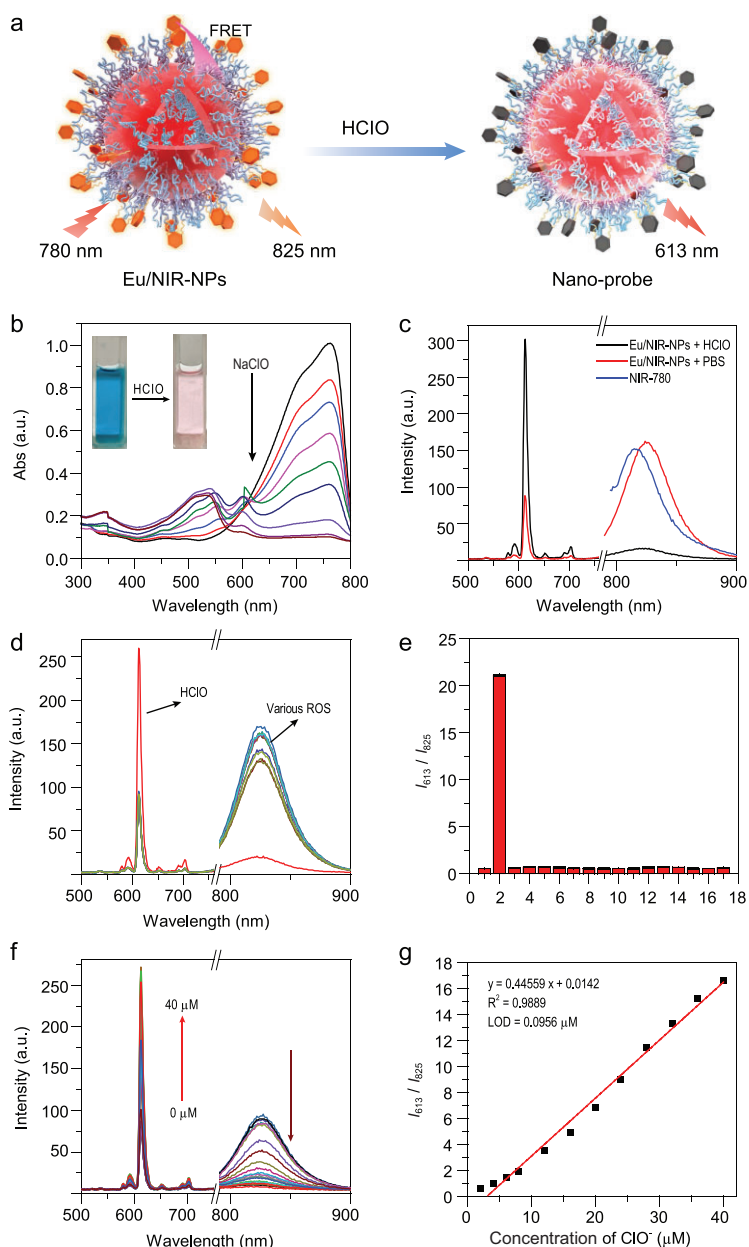


Figure 4. (a) Schematic illustration of Eu/NIR-NPs detecting HClO. (b) The UV-vis spectra of Eu/NIR-NPs in different concentrations of HClO in water media. (Inset: photographs of Eu/NIR-NPs solution before or after adding NaClO.) (c) The fluorescence spectra of Eu/NIR-NPs, IR-780 and Eu/NIR-NPs with NaClO. (d) Fluorescence spectra of Eu/NIR-NPs (1.0 mg/mL) after adding 40.0 μM of various ROS and NaClO in HEPES buffer solution (10 mM, pH 7.4). (e) The competing responses of Eu/NIR-NPs to various substances and NaClO in HEPES buffer solution (10 mM, pH = 7.4). (1) PBS, (2) NaClO, (3) $\cdot\text{OH}$, (4) $^1\text{O}_2$, (5) NO, (6) ONOO $^-$, (7) t-BuOOH, (8) H_2O_2 , (9) GSH, (10) Cys, (11) Glu, (12) PO_4^{3-} , (13) CO_3^{2-} , (14) HS^- , (15) Cl^- , (16) SO_4^{2-} , (17) NO_2^- , (18) NO_3^- . $\lambda_{\text{ex}} = 780 \text{ nm}$. (f) Fluorescence response of Eu/NIR-NPs (1.0 mg/mL) towards NaClO (0–40.0 μM). (g) The linear relationship between the fluorescence ratio (I_{613}/I_{825}) and different NaClO concentrations (from 0 to 40.0 μM). $\lambda_{\text{ex}} = 780 \text{ nm}$.

in this assembly, and IR-780 was used as energy acceptor (Figs S16 and S17). First, we studied the assembly and fluorescence properties with different ratios of Eu(THB)(THA) $_2$ Phen and

NIR-780. When the donor/acceptor pair were co-assembled as one nanoprobe, intermolecular FRET occurred, and the phosphorescence intensity of Eu(THB)(THA) $_2$ Phen decreased (Fig. S18). Based on its good spectral properties, we chose Eu(THB)(THA) $_2$ Phen and IR-780 at the ratio of 50/7 as the nanoprobe for detecting HClO. Here, the RE complex Eu(THB)(THA) $_2$ Phen displayed efficient two-photon-sensitized and high-purity red emission. Moreover, it can emit characteristic fluorescence of Eu^{3+} under 780 nm excitation, and IR-780 can also be effectively excited by 780 nm wavelength. Therefore, we chose 780 nm excitation to observe the ratio changes in fluorescence. Due to the specific and fast recognition of hypochlorous acid by NIR-780, the absorption of IR-780 slowly decreased with the addition of HClO (Fig. 4b), and the luminescence intensity of Eu(THB)(THA) $_2$ Phen increased (Fig. 4c). The lifetime of Eu/NIR-NPs was 360.45 μs (decay time at 613 nm emission). After adding HClO, the lifetime increased to 698.32 μs (Fig. S19).

As shown in Fig. 4d and e, the addition of other ROS ($\cdot\text{OH}$, $^1\text{O}_2$, NO, ONOO $^-$, t-BuOOH, H_2O_2) or substances (GSH, Cys, Glu, PO_4^{3-} , CO_3^{2-} , HS^- , Cl^- , SO_4^{2-} , NO_2^- , NO_3^-) did not cause a significant change in the fluorescence intensity of Eu/NIR-NPs in the aqueous solution. After adding HClO, the fluorescence of Eu/NIR-NPs changed obviously. The emission titration spectra of Eu/NIR-NPs towards HClO were measured (Fig. 4f). Under two-photon excitation at 780 nm, the change in the fluorescence intensity ratio I_{613}/I_{825} with HClO concentration had a good linear relationship. The linear relationship between HClO and I_{613}/I_{825} could be fitted as a function of equation (7),

$$I_{613}/I_{825} = 0.44559x + 0.01424, \quad (7)$$

with a correlation coefficient (R^2) of 0.989 (Fig. 4g). The limit of detection (LOD) of HClO was calculated to be 95.60 nM with the formula $3s/k$. Overall, these results clearly demonstrated that Eu/NIR-NPs acted as nanoprobe with excellent selectivity and anti-interference ability, and could effectively identify HClO using fluorescence signal ratio I_{613}/I_{825} under two-photon excitation.

Cytotoxicity and confocal fluorescence imaging in living cells

Since the nanoprobe Eu^{3+} -NPs-0.5 are dispersed nanospheres with a particle size of less than 100 nm, and also show a positive potential of +35 eV, we expect that they can target mitochondria in

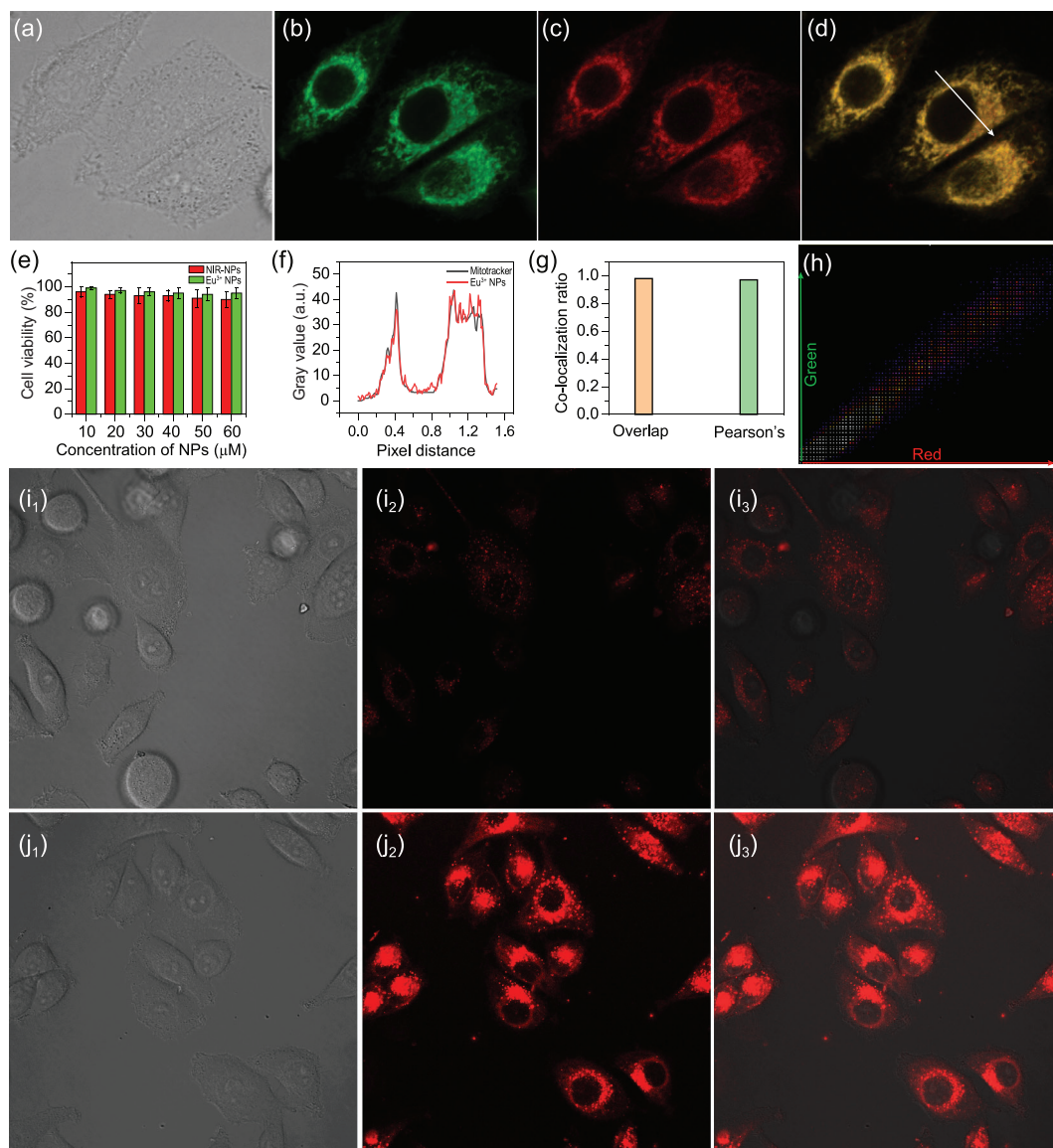


Figure 5. Confocal imaging photos of HeLa cells co-incubated with Eu^{3+} -NPs ($\lambda_{\text{ex}} = 405 \text{ nm}$; $\lambda_{\text{em}} = 600\text{--}630 \text{ nm}$) and Mitotracker red ($\lambda_{\text{ex}} = 641 \text{ nm}$; $\lambda_{\text{em}} = 650\text{--}670 \text{ nm}$) for 30 min at 37°C . (a) Bright-field images; (b) Mitotracker red, $\lambda_{\text{ex}} = 641 \text{ nm}$ and $\lambda_{\text{em}} = 650\text{--}670 \text{ nm}$; (c) Eu^{3+} -NPs, $\lambda_{\text{ex}} = 405 \text{ nm}$ and $\lambda_{\text{em}} = 600\text{--}630 \text{ nm}$. (d) Merged images. (e) MTT assays for HeLa cells incubated with Eu-NPs and NIR NPs. (f) Intensity profile of chosen regions (white arrow in Fig. 5d) across HeLa cells. (g) Pearson's coefficient and overlap coefficient. (h) Co-localization areas displayed of the red and green channels selected in Fig. 5d. Fluorescence images of HeLa cells incubated with (i) $10 \mu\text{M}$ of Eu/NIR-NPs for 1 h, (j) $10 \mu\text{M}$ of Eu/NIR-NPs for 1 h and further incubated for another 30 min with HClO. (1) Bright-field images. (2) Fluorescence channel images. (3) Merged images. $\lambda_{\text{ex}} = 780 \text{ nm}$; $\lambda_{\text{em}} = 600\text{--}630 \text{ nm}$.

living cells [46–48]. To confirm the hypothesis, we utilized co-localization experiments of Eu^{3+} -NPs and Mitotracker red to describe the difference between their locations in mitochondria [49,50]. As shown in Fig. 5a–c, the living HeLa cells were costained with $5 \mu\text{M}$ Mitotracker red (a mitochondria dye, 30 min) and $10 \mu\text{M}$ Eu^{3+} -NPs (30 min). The intensity profiles of Eu^{3+} -NPs and Mitotracker red (640/665 nm) emissions in the linear region

(white arrow in Fig. 5d) across HeLa cells varied in close synchrony (Fig. 5f). Besides, the fluorescence of Eu^{3+} -NPs overlapped well with the red fluorescence of Mitotracker red (overlapping $>98\%$ and Pearson's correlation coefficient $>90\%$) (Fig. 5g and h). All the above results verified that Eu^{3+} -NPs possessed excellent ability to locate into mitochondria. Besides, the cytotoxicity was determined using MTT as an indicator. Even when

Eu³⁺-NPs concentration was as high as 60 μM, 95% of the cells remained viable, which indicated that Eu³⁺-NPs had good biocompatibility and low cytotoxicity (Fig. 5e).

To further assess the biological application of Eu/NIR-NPs, two-photon fluorescence imaging for HClO detection was carried out in living HeLa cells. Under two-photon excitation, distinguishable fluorescence was generated in living cells and detected in real time. As described in Fig. 5i, cells treated only with Eu/NIR-NPs for 1 h at 37°C emitted a correspondingly weak luminescence emission in red channels under excitation at 780 nm. Nevertheless, when the same cells were treated with 50 μM of HClO for 0.5 h, a strong red luminescence signal was observed inside living cells (Fig. 5j). These results indicated that Eu/NIR-NPs could penetrate into cells and react with HClO in living cells.

CONCLUSION

In summary, a new strategy was proposed to obtain Eu-NPs with SAIL characteristics. By systematically studying its self-assembly and optical properties in aqueous solution, it was found that the Eu³⁺-complex can be self-assembled into spherical nanoparticles in an aqueous solution while having the property of SAIL. Based on its efficient self-assembly in aqueous solution, we also studied its temperature-sensing properties by measuring the steady-state fluorescence and transient fluorescence changes at different temperatures. Experimental results indicated that Eu-NPs-0.5 as a fluorescence lifetime thermal sensor or luminescent sensor for temperature performed better than other reported thermal probes based on RE materials in terms of its maximum relative sensitivity. Finally, we successfully constructed a FRET system through co-assembly of the Eu³⁺-complex and IR-780. It was used as a ratiometric two-photon fluorescent probe to achieve sensitive and selective detection of hypochlorous acid in aqueous solution and living cells. We believe that the SAIL activity of the RE system proposed here offers a further step forward in the development of RE light conversion systems and their integrated applications in bioimaging and therapy.

SUPPLEMENTARY DATA

Supplementary data are available at [NSR](#) online.

FUNDING

This work was supported by the National Natural Science Foundation of China (21931001, 21871121 and 21971097), the

Special Fund Project of Guiding Scientific and Technological Innovation Development of Gansu Province (2019ZX-04) and the 111 Project (B20027).

AUTHOR CONTRIBUTIONS

Y.T. and C.-H.Y. conceived this project. Y.T. and P.S. designed the experiments. P.S. conducted all the experiments and characterizations. T.W., M.Z. and L.L. performed the fluorescence test and biological imaging. P.Z. collected relevant calculation data. Y.T., P.S., X.Y. and X.F. performed the analysis with constructive discussions. All authors contributed to discussing the results and writing the manuscript.

Conflict of interest statement. None declared.

REFERENCES

- Feng J and Zhang HJ. Hybrid materials based on lanthanide organic complexes: a review. *Chem Soc Rev* 2013; **42**: 387–410.
- Wang XH, Chang HJ and Xie J *et al.* Recent developments in lanthanide-based luminescent probes. *Coord Chem Rev* 2014; **273**: 201–12.
- Xu JT, Gulzar A and Yang PP *et al.* Recent advances in near-infrared emitting lanthanide-doped nanoconstructs: mechanism, design and application for bioimaging. *Coord Chem Rev* 2019; **381**: 104–34.
- Zhao ZF, Wang LW and Zhan G *et al.* Efficient rare earth cerium(III) complex with nanosecond d–f emission for blue organic light-emitting diodes. *Natl Sci Rev* 2021; **8**: nwaa193.
- Zhao YW, Zhang FQ and Zhang XM. Single component lanthanide hybrids based on metal-organic framework for near-ultraviolet white light LED. *ACS Appl Mater Interfaces* 2016; **8**: 24123–30.
- Ren W, Lin GG and Clarke C *et al.* Optical nanomaterials and enabling technologies for high-security-level anticounterfeiting. *Adv Mater* 2020; **32**: 1901430.
- Yang YW, Su PR and Tang Y. Stimuli-responsive lanthanide-based smart luminescent materials for optical encoding and bio-applications. *Chem Nano Mat* 2018; **4**: 1097–120.
- Amoroso AJ and Pope SJA. Using lanthanide ions in molecular bioimaging. *Chem Soc Rev* 2015; **44**: 4723–42.
- Monteiro J. Recent advances in luminescence imaging of biological systems using lanthanide(III) luminescent complexes. *Molecules* 2020; **25**: 2089.
- Deng Z, Huang J and Xue Z *et al.* A general strategy for designing NIR-II emissive silk for the in vivo monitoring of an implanted stent model beyond 1500 nm. *J Mater Chem B* 2020; **8**: 4587–92.
- Mini P, Springer MA and Grace MR *et al.* A highly efficient red-emitting luminescent paper-based chemosensor for hydrogen sulfide. *Chem Commun* 2020; **56**: 5605–8.
- Andresen E, Wurth C and Prinz C *et al.* Time-resolved luminescence spectroscopy for monitoring the stability and dissolution behaviour of upconverting nanocrystals with different surface coatings. *Nanoscale* 2020; **12**: 12589–601.

13. Brennecke B, Wang QH and Zhang QY *et al.* An activatable lanthanide luminescent probe for time-gated detection of nitroreductase in live bacteria. *Angew Chem Int Ed* 2020; **59**: 8512–6.
14. Eliseeva SV and Bünzli JCG. Lanthanide luminescence for functional materials and bio-sciences. *Chem Soc Rev* 2010; **39**: 189–227.
15. de Bettencourt-Dias A, Barber PS and Bauer S. A water-soluble pybox derivative and its highly luminescent lanthanide ion complexes. *J Am Chem Soc* 2012; **134**: 6987–94.
16. Kovacs D, Mathieu E and Kiraev SR *et al.* Coordination environment-controlled photoinduced electron transfer quenching in luminescent europium complexes. *J Am Chem Soc* 2020; **142**: 13190–200.
17. Li QR, Song SH and Feng ZY *et al.* Luminescent vesicles self-assembled directly from an amphiphilic europium complex in an ionic liquid. *Langmuir* 2020; **36**: 2911–9.
18. Reichert WM, Holbrey JD and Vigour KB *et al.* Approaches to crystallization from ionic liquids: complex solvents-complex results, or, a strategy for controlled formation of new supramolecular architectures? *Chem Commun* 2006; **34**: 4767–79.
19. Nakamura K, Hasegawa Y and Kawai H *et al.* Enhanced lasing properties of dissymmetric Eu(III) complex with bidentate phosphine ligands. *J Phys Chem A* 2007; **111**: 3029–37.
20. Harada T, Tsumatori H and Nishiyama K *et al.* Nona-coordinated chiral Eu(III) complexes with stereoselective ligand-ligand noncovalent interactions for enhanced circularly polarized luminescence. *Inorg Chem* 2012; **51**: 6476–85.
21. Xie YJ and Li Z. Approaching aggregated state chemistry accelerated by aggregation-induced emission. *Natl Sci Rev* 2021; **8**: nwaa199.
22. Liu QQ, Liu YD and Yin YD. Optical tuning by the self-assembly and disassembly of chain-like plasmonic superstructures. *Natl Sci Rev* 2018; **5**: 128–30.
23. Xu W, Yu YG and Ji XN *et al.* Self-stabilized amorphous organic materials with room-temperature phosphorescence. *Angew Chem Int Ed* 2019; **58**: 16018–27.
24. Li DF, Lu FF and Wang J *et al.* Amorphous metal-free room-temperature phosphorescent small molecules with multicolor photoluminescence via a host-guest and dual-emission strategy. *J Am Chem Soc* 2018; **140**: 1916–23.
25. Ma X, Wang J and Tian H. Assembling-induced emission: an efficient approach for amorphous metal-free organic emitting materials with room temperature phosphorescence. *Acc Chem Res* 2019; **52**: 738–48.
26. Zhao Z, Zhang HK and Lam JWY *et al.* Aggregation-induced emission: new vistas at the aggregate level. *Angew Chem Int Ed* 2020; **59**: 9888–907.
27. Ning YY, Zhu ML and Zhang JL. Near-infrared (NIR) lanthanide molecular probes for bioimaging and biosensing. *Coord Chem Rev* 2019; **399**: 213028.
28. Liu J, Morikawa MA and Kimizuka N. Conversion of molecular information by luminescent nanointerface self-assembled from amphiphilic Tb(III) complexes. *J Am Chem Soc* 2011; **133**: 17370–4.
29. Zhang GP, Zhu HX and Chen MJ *et al.* Aggregation-induced emission of Eu-III complexes balanced with bulky and amphiphilic imidazolium cations in ethanol/water binary mixtures. *Chem-Eur J* 2018; **24**: 15912–20.
30. Lewis RW, Malic N and Saito K *et al.* Ultra-high molecular weight linear coordination polymers with terpyridine ligands. *Chem Sci* 2019; **10**: 6174–83.
31. Morikawa M, Tsunofuri S and Kimizuka N. Controlled self-assembly and luminescence characteristics of Eu(III) complexes in binary aqueous/organic media. *Langmuir* 2013; **29**: 12930–5.
32. Li ZQ, Hou ZH and Fan HX *et al.* Organic-inorganic hierarchical self-assembly into robust luminescent supramolecular hydrogel. *Adv Funct Mater* 2017; **27**: 1604379.
33. Li YW, Dong YH and Cheng L *et al.* Aggregation-induced emission and light-harvesting function of tetraphenylethene-based tetracationic dicyclophane. *J Am Chem Soc* 2019; **141**: 8412–5.
34. Kitagawa Y, Kumagai M and Nakanishi T *et al.* First aggregation-induced emission of a Tb(III) luminophore based on modulation of ligand-ligand charge transfer bands. *Dalton Trans* 2020; **49**: 2431–6.
35. Zhang Y, Shen TT and Kirillov AM *et al.* NIR light/H₂O₂-triggered nanocomposites for a highly efficient and selective synergistic photodynamic and photothermal therapy against hypoxic tumor cells. *Chem Commun* 2016; **52**: 7939–42.
36. Li WL, Wang J and Xie YX *et al.* Water-based fluorescent paint: presenting a novel approach to study and solve the aggregation caused quench (ACQ) effect in traditional fluorescent materials. *Prog Org Coat* 2018; **120**: 1–9.
37. Beeby A, Clarkson IM and Dickins RS *et al.* Non-radiative deactivation of the excited states of europium, terbium and ytterbium complexes by proximate energy-matched OH, NH and CH oscillators: an improved luminescence method for establishing solution hydration states. *J Chem Soc, Perkin Trans* 1999; **2**: 493–504.
38. Quici S, Cavazzini M and Marzanni G *et al.* Visible and near-infrared intense luminescence from water-soluble lanthanide Tb(III), Eu(III), Sm(III), Dy(III), Pr(III), Ho(III), Yb(III), Nd(III), Er(III) complexes. *Inorg Chem* 2005; **44**: 529–37.
39. Werts MHV, Jukes RTF and Verhoeven JW. The emission spectrum and the radiative lifetime of Eu³⁺ in luminescent lanthanide complexes. *Phys Chem Chem Phys* 2002; **4**: 1542–8.
40. Sabbatini N, Guardigli M and Lehn JM. Luminescent lanthanide complexes as photochemical supramolecular devices. *Coord Chem Rev* 1993; **123**: 201–28.
41. Brites CDS, Lima PP and Silva NJO *et al.* Thermometry at the nanoscale. *Nanoscale* 2012; **4**: 4799–829.
42. Zhu S and Gu ZJ. Temperature-feedback upconversion nanocomposite creates a new strategy for photothermal therapy. *Sci Bull* 2017; **62**: 229–30.
43. Yu ZZ, Hu WB and Zhao H *et al.* Generating new cross-relaxation pathways by coating prussian blue on NaNdF₄ to fabricate enhanced photothermal agents. *Angew Chem Int Ed* 2019; **58**: 8536–40.
44. Zhan ZX, Su ZS and Chai L *et al.* Multimodal imaging iridium(III) complex for hypochlorous acid in living systems. *Anal Chem* 2020; **92**: 8285–91.
45. Wu LL, Huang CS and Emery B *et al.* Förster resonance energy transfer (FRET)-based small-molecule sensors and imaging agents. *Chem Soc Rev* 2020; **49**: 5110–39.
46. Wang X, Sun J and Zhang WH *et al.* A near-infrared ratiometric fluorescent probe for rapid and highly sensitive imaging of endogenous hydrogen sulfide in living cells. *Chem Sci* 2013; **4**: 2551–6.
47. Gao P, Pan W and Li N *et al.* Fluorescent probes for organelle-targeted bioactive species imaging. *Chem Sci* 2019; **10**: 6035–71.
48. Weissleder R, Kelly K and Sun EY *et al.* Cell-specific targeting of nanoparticles by multivalent attachment of small molecules. *Nat Biotechnol* 2005; **23**: 1418–23.
49. Yu FB, Li P and Wang BS *et al.* Reversible near-infrared fluorescent probe introducing tellurium to mimetic glutathione peroxidase for monitoring the redox cycles between peroxynitrite and glutathione in vivo. *J Am Chem Soc* 2013; **135**: 7674–80.
50. Luo S, Tan X and Fang S *et al.* Mitochondria-targeted small-molecule fluorophores for dual modal cancer phototherapy. *Adv Funct Mater* 2016; **26**: 2826–35.